Scientific Reports

https://doi.org/10.1038/s41598-026-46908-w

Article in Press

Numerical and experimental analysis of flow distortion induced by ultrasonic transducers in gas flowmeters

Received: 26 January 2026

Accepted: 27 March 2026

Published online: 03 April 2026

Cite this article as: Chen W., Yao C., Wang D. *et al.* Numerical and experimental analysis of flow distortion induced by ultrasonic transducers in gas flowmeters. *Sci Rep* (2026). https://doi.org/10.1038/s41598-026-46908-w

Wenlin Chen, Cunxin Yao, Duoyong Wang, Jun Mu, Chao Xu & Defu Xu

Numerical and Experimental Analysis of Flow Distortion Induced by Ultrasonic Transducers in Gas Flowmeters

Wenlin Chen[1,2,3*],Cunxin Yao[4], Duoyong Wang[4], Jun Mu[1], Chao Xu[3], Defu Xu[2]

[1] China Merchants Xinjiang institute of Measurement and Testing Technology co., Ltd, Urumqi 830011, China
[2] Xinjiang Institute of Measurement & Testing Technology, Urumqi 830011, China
[3] Tianjin University·, Tianjin 300072, China,
[4] Xinjiang Gas Group Co., Ltd·, Urumqi 830011, China
(Corresponding author email: chenwenlin@cmhk.com)

Abstract

This study investigates the flow field distribution near the transducer and quantifies the distortion of the velocity profile along ultrasonic paths. It elucidates the physical mechanisms through which flow separation—induced by the mainstream flow around the transducer—affects ultrasonic flowmeter measurements. Experimental analyses examine the influence of localized flow field distortion under various pressures and flow rates, leading to the development of an error correction model consistent with empirical data. Numerical simulations are performed for three transducer installation modes: fully projecting, fully recessed, and tangent, revealing the distinct physical mechanisms associated with each configuration. Measurement errors are consistently negative due to the effects of backflow and lateral flow. Error ranges are -1.86% to -1.15% for fully projecting, -4.09% to -2.26% for tangent, and -10.57% to -9.66% for fully recessed installations, indicating that the fully recessed mode introduces the most significant flow disturbance. Flow velocity correction models are proposed for each installation type. After modification, errors are largely confined within ±1.0% for both fully projecting and fully recessed transducers. The effect of local flow distortion on tangent-type ultrasonic flowmeters is further examined through experiments under varying pressures and flow velocities. By applying a secondary correction model based on Reynolds number, measurement accuracy can achieve the ±0.5% standard.

Key words

ultrasonic flowmeter, transducer installation effect, flow separation, local flow field distortion, error correction model.

1. Introduction

In recent years, ultrasonic flowmeters have undergone rapid development owing to their numerous advantages, including no moving parts, low pressure loss, broad measurement range, and high accuracy. The growing interest in ultrasonic flowmeters within the gas industry is evidenced by A.G.A Report No. 9[1]. The intrusion of transducers into pipelines affects ultrasonic flow measurement in two primary ways[2]: firstly, by altering the acoustic path length due to transducer insertion into the pipe wall, and secondly, by disturbing the local flow field around the transducers[3]. Correction factors can be applied to individual paths to mitigate these effects[4]. The measurement uncertainty of ultrasonic flowmeters is influenced by factors such as Reynolds number[5], pipe diameter, transducer dimensions, and installation configuration (e.g., projecting or recessed).

As specified in IEC 60041 (Field acceptance tests to determine the hydraulic performance of hydraulic turbines, storage pumps, and pump-turbines)[6], the protrusion or recession of transducers on the inner pipeline wall has a significant impact on the accuracy of ultrasonic flowmeters. Specifically, projecting transducers reduce both the acoustic path length and the local flow velocity, leading to negative measurement errors. In contrast, recessed transducers cause flow field distortion due to the presence of wall grooves. The standard requires that computational fluid dynamics (CFD) analysis or hydraulic testing be conducted if the ratio of transducer protrusion to acoustic path length exceeds 0.25%.

In IEC 60041, some analysis has been provided for large-diameter pipes; however, scenarios involving acoustic path lengths shorter than 1 meter are not addressed. Moreover, the influence of flow disturbances—caused by recessed and tangent transducer installation—on the measurement accuracy of ultrasonic flowmeters remains unanalyzed. Current research predominantly focuses on ultrasonic flowmeters with large diameters[7-9], while studies on measurement errors induced by insertion-type transducers in small and medium-diameter pipelines remain limited[10-12].

While wet-calibration is the standard industrial practice for determining overall meter accuracy by directly establishing calibration factors across a range of Reynolds numbers, this approach treats the flowmeter as an integrated system and does not isolate the contribution of individual physical phenomena. Understanding the underlying mechanisms of transducer-induced flow distortion is essential for several reasons: (1) it enables a more physically-informed optimization of transducer geometry and placement, (2) it provides a basis for developing correction models that could reduce the extent of required calibration, and (3) it helps predict meter performance under operating conditions that may not be fully covered by the calibration envelope. This study aims to bridge this gap by investigating these physical mechanisms.

This study investigates the flow field distribution near the transducers and alterations in the velocity profile along ultrasonic paths[13] to elucidate the physical mechanisms behind measurement errors caused by flow separation. Experimental validation under various pressure and flow rate conditions quantifies the influence of localized flow-field distortions. By combining CFD simulations with empirical validation, this work bridges a key research gap through the development and validation of error correction models specifically designed to account for transducer installation effects.

2. Numerical simulation modeling and meshing of local flow field distortion around transducers

2.1 Model Construction

Simplified models of an ultrasonic flowmeter with different transducer installation configurations were developed in ICEM. Three installation modes were considered: (a) fully projecting, (b) tangent, and (c) fully recessed. As shown in Figure 1d and Table 1, the acoustic path length varies considerably among these configurations. The pipeline has a diameter of 100 mm, and the flowmeter body section has a length of 3D. To ensure fully developed flow, a 10D straight inlet section and a 5D straight outlet section were incorporated. The transducer diameter is 12 mm, and the path line forms a 60° angle θ with the pipe axis. This 60° angle was selected because it is a common industrial standard for multi-path ultrasonic gas flowmeters, offering a well-established compromise between acoustic path length (which affects time-of-flight resolution) and sensitivity to the axial velocity component. While larger angles (e.g., 75°) could potentially reduce the downstream separation region, they would also compress the effective velocity measurement range. A systematic parametric study of installation angles is beyond the scope of the current work, but it represents a valuable direction for future research.

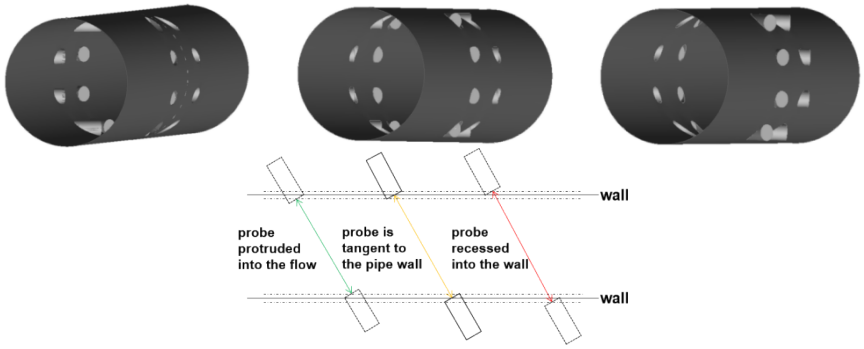

a. fully projecting b. tangent c. fully recessed d. transducer insertion depth

Figure 1 Schematic of transducer installation modes.

Table 1 Path length under different installation methods

Installation method	Path No.	Path length (mm)
fully projecting	1(4)	42.5

tangent	2(3)	100.7
	1(4)	67.9
	2(3)	109.8
fully recessed	1(4)	86.4
	2(3)	117.9

The path positions are determined in accordance with the Gauss-Jacobi integration scheme, as summarized in Table 2. The mean velocity over the cross-section is obtained through a weighted summation of the velocities measured along each individual path. It is important to note that the Gauss-Jacobi quadrature assumes an ideal velocity profile, i.e., a uniform velocity distribution across the pipe cross-section. The weighting factors and path positions are derived based on a half-circle area flow function, which corresponds to the assumption of uniformity. While this method is widely adopted in industrial ultrasonic flowmeter applications, more advanced integration schemes such as OWICS (Optimized Weights for Circular Section) can provide improved accuracy by accounting for more realistic velocity profiles. However, the primary focus of this study is to quantify the physical mechanisms of transducer-induced flow distortion rather than to optimize the integration scheme. Any deviation from the ideal flow assumption, such as the distortions investigated here, will lead to measurement errors. The negative measurement errors we report are a direct consequence of the real, distorted flow field, which contrasts with the ideal assumption of the integration method.

Any deviation from this ideal flow, such as the transducer-induced distortions investigated in this study, will lead to measurement errors. The negative measurement errors we report are a direct consequence of the real, distorted flow field, which contrasts with the ideal assumption of the integration method. For a single measurement section, the flow rate is calculated using Equation 1[14, 15]. In this equation, K denotes the flow rate correction factor, D is the internal diameter of the meter, w_i represents the Gauss-Jacobi weighting factor corresponding to path i, v_i is the mean velocity along path i, L_{wi} indicates the geometric length of the acoustic path from pipe wall to wall, and K' refers to the velocity correction factor. The velocity weighting factor W_i can be determined using the Gauss-Jacobi quadrature integration method[16]. In the case of two-section measurement, the final flow rate is taken as the average of the volumetric flow rates obtained from both sections. To avoid ambiguity, we define the key geometric parameters as follows: L_i: The length of the acoustic path between the transducer faces. L_{wi}: The geometric length of the acoustic path from pipe wall to pipe wall.

To minimize integration errors, an ideal ultrasonic flowmeter with the same path configuration is assumed to be positioned 2D upstream of the transducer installation section. Reference values are obtained from this idealized setup. The measurement error is defined by Equation 2, in which Q_{ref} denotes the flow rate under reference conditions.

$$Q = K\frac{D}{2}\sum_{i=1}^{n} w_i v_i L_{wi}\sin\theta = K'\frac{\pi D^2}{4}\sum_{i=1}^{n} W_i v_i \tag{1}$$

$$E = \frac{Q - Q_{ref}}{Q_{ref}} \times 100\% \tag{2}$$

Table 2 Integral parameters of ultrasonic flowmeter corresponding to Gauss-Jacobi method

Path No.	path height ratio d_i	Weight factor of flow rate w_i	Weight factor of velocity W_i
1	0.8090	0.3693	0.1382
2	0.3090	0.5976	0.3618
3	-0.3090	0.5976	0.3618
4	-0.8090	0.3693	0.1382

2.2 Meshing and calculation parameter settings

The fluid domain was discretized using a tetrahedral hybrid mesh. To accurately capture the high-velocity gradients and flow separation phenomena near the transducer surfaces, boundary-layer refinement was applied in these regions. The boundary-layer mesh consisted of 15 prismatic layers, with the first-layer height carefully controlled to ensure a wall $y+$ value between 1 and 5, thereby satisfying the near-wall resolution requirement of the SST k-ω turbulence model. A grid independence study was conducted, resulting in a final mesh of approximately 1.5 million elements. This approach not only enhanced the grid resolution in regions with strong gradients, particularly in the wake of the transducers, but also maintained computational efficiency by keeping the total cell count manageable.

Flow separation within the wedge-shaped flow field of the ultrasonic transducer is a key operational characteristic. Owing to its strong capability in predicting separated flows, the SST k-omega turbulence model[14] was adopted. Heat transfer between the fluid and the external environment was assumed negligible. A second-order upwind scheme was employed for spatial

discretization, and the SIMPLEC algorithm was used for pressure–velocity coupling. The fluid properties were set to approximate those of air at 0.36 MPa and 300 K. This pressure level was chosen specifically to match the operating conditions of our in-house high-pressure flow calibration facility, enabling direct and meaningful validation of the CFD results against experimental data. The inlet boundary was defined as a velocity inlet, with velocities ranging from 1 m/s to 30 m/s, while the outlet was specified as an outflow condition. The wall roughness was set to 0.2 mm. To ensure a fully developed flow at the measurement section, a fully developed velocity profile—including distributions of mean velocity, turbulent kinetic energy (k), and specific dissipation rate (ω)—was imposed at the inlet. This profile was obtained from a separate precursor simulation of a long straight pipe with a length of 50D, ensuring that the boundary layer and turbulence characteristics were fully developed before entering the main computational domain. To verify that the imposed fully developed profile is maintained throughout the domain, we monitored the wall static pressure along the axial distance upstream of the measurement section. The pressure decay is linear, and the corresponding friction factor agrees well with theoretical predictions for the given Reynolds numbers, confirming that the flow remains fully developed.

Based on the above setup, detailed velocity data for each acoustic path could be obtained. The layout and numbering of the parallel paths are shown in Figure 3, with paths 1 to 4 arranged sequentially from top to bottom. For a single path, as illustrated in Figure 2, the mean axial velocity components are given by Equation 3, where L_i denotes the length of path i. The instantaneous velocity components along the path are denoted as v_{xi}, v_{yi}, and v_{zi}. Accordingly, the average velocity along path i can be calculated using Equation 4, where $\beta = 60°$, $\alpha = 30°$, $\gamma = 90°$.

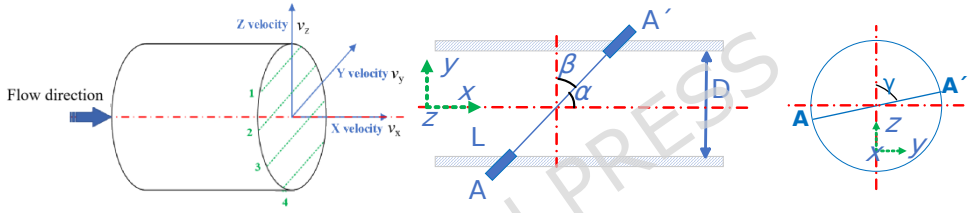

Figure 2 The angle between parallel path arrangement and each axial direction.

$$V_{xi} = \frac{1}{L_i}\int_A^{A'} v_{xi}\,dL,\ V_{yi} = \frac{1}{L_i}\int_A^{A'} v_{yi}\,dL,\ V_{zi} = \frac{1}{L_i}\int_A^{A'} v_{zi}\,dL \tag{3}$$

$$V = V_x + V_y\frac{\cos\beta}{\cos\alpha} + V_z\frac{\cos\beta}{\cos\gamma} = V_x + V_y\frac{\cos\beta}{\cos\alpha} = V_x + V_y\tan\beta \tag{4}$$

The path velocities were evaluated using the following approach: For each acoustic path, we extracted velocity data along a line defined by the path geometry using 2000 equally spaced sampling points. At each point, the velocity components were interpolated from the surrounding mesh elements using second-order accurate inverse distance weighting. The path-averaged velocity was then computed by numerically integrating these interpolated values along the path length using the trapezoidal rule. The no-slip condition at the wall (zero velocity) was properly enforced at the path endpoints.

To estimate the uncertainty of this integration method, we conducted a sensitivity study by varying the number of sampling points from 500 to 5000. The variation in the integrated path velocity was found to be less than 0.15% for all paths when using more than 1500 points, confirming that our choice of 2000 points provides a sufficiently grid-independent result. This integration uncertainty is considerably smaller than the numerical discretization uncertainty (approximately 1.0%) and the experimental uncertainty (0.20%), and therefore does not significantly affect the overall conclusions of this study.

3. Analysis of numerical simulation results

3.1 Verification of Simulation Results

To validate the reliability of the CFD simulations, a comparison was conducted between the simulated and experimental flow measurements under the tangent transducer installation mode. As shown in Table 3, the simulation data are compared with experimental results at inlet velocities of 4 m/s and 15 m/s.

3.1.1 Uncertainty Analysis

A detailed uncertainty analysis was performed for both the experimental and numerical results to provide context for the verification. The experimental reference flow facility is a high-pressure closed-loop gas standard with a calibrated expanded uncertainty of U_{rel} = 0.20%

(k=2) , as determined from its most recent accreditation. The numerical uncertainty was estimated by following the Grid Convergence Index (GCI) method based on three systematically refined meshes (coarse, medium, and fine). The discretization uncertainty for the integrated flow rate was found to be approximately 1.0% . Iterative convergence was ensured by reducing residuals to below 10^{-5}.

As shown in Table 3, the simulation yields errors of -2.88% and -2.62% at 4 m/s and 15 m/s, respectively, while the experiment yields -1.49% and -2.27%. The discrepancies between simulation and experiment can be attributed primarily to two factors: (1) simplifications in the geometric model, particularly the omission of radial grooves and rounded edges on the transducer, and (2) inherent assumptions and limitations of the RANS turbulence model in capturing the precise dynamics of complex, unsteady separated flows. Considering the combined uncertainty bands, the numerical results are considered to be in acceptable agreement with the experimental data, confirming the validity of the simulation approach for capturing the dominant flow physics.

Table 3 Comparison between simulation results and experimental results

Results	Velocity (m/s)	Calculated flow rate (m^3/h)	Reference flow (m^3/h)	E (%)
Simulation	4	135.92	139.95	□2.88
Experiment		108.20	109.84	□1.49
Simulation	15	404.10	414.97	□2.62
Experiment		394.59	403.75	□2.27

3.2 Comparative analysis of flow field distributions for different transducer installation methods

3.2.1 Fully Projecting mode

In the fully projecting installation mode, the transducer protrudes entirely from the pipe wall into the flow, forming a wedge-shaped obstruction with an OMNP node, as shown in Figure 3. The region of the flow field downstream of the transducer that most significantly affects measurement accuracy is the cylindrical area bounded by the end faces of the upstream and downstream transducers, outlined by the dashed box in Figure 4. When the viscous fluid reaches point O, it is forced to accelerate upward along the wedge surface, resulting in a climbing flow. As the fluid moves from point O to point M, its velocity increases markedly while the pressure decreases significantly, that is $\frac{dp}{dx}$□0.

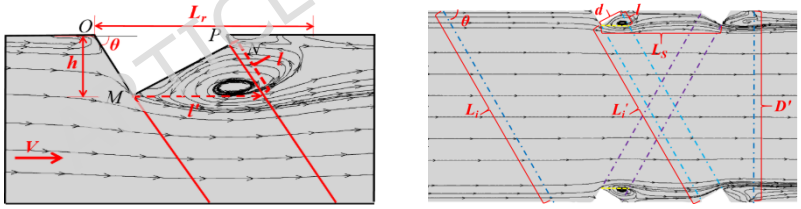

Figure 3 Schematic diagram of transducer measuring area and path length of the fully projecting type

The pressure gradient-induced force drives the fluid forward, initiating a flow process marked by depressurization and acceleration. During this stage, only the surface viscous resistance acts against the direction of fluid motion. While this resistance reduces the flow velocity, it does not reverse the flow direction, thus preventing boundary layer separation. As the climbing flow reaches point M, the potential flow achieves its maximum velocity at this location, here dp/dx□0. Beyond point M, the pressure begins to rise, there is dp/dx□0, and the magnitude of the adverse pressure gradient increases gradually with x. When the fluid approaches point N, the combined influence of the adverse pressure gradient and viscous effects near the surface causes the near-wall fluid to decelerate continuously. The fluid eventually stagnates as inertial forces can no longer overcome these resistive effects. Consequently, the flow within the boundary layer separates from the transducer surface, resulting in vortex formation behind the transducer and backflow at its upstream end.

The energy loss due to flow resistance within the boundary layer leads to a pressure drop at point N relative to point O. As a result, cavitation is prone to occur downstream of the transducer after boundary layer separation. In practical applications, these low-velocity recirculation zones can also promote the accumulation of debris and contaminants on the transducer surface. Over time, this contamination can alter the transducer's acoustic properties or its geometric profile, potentially leading to a gradual drift in metrological characteristics. This extends the practical relevance of our findings to long-term field operation.

Figure 4 shows the flow field distribution and normalized velocity across multiple paths under the fully projecting transducer installation mode. The reference velocity is obtained by integrating the velocity profile over the cross-section at a plane located 2D upstream of the transducer section, where the flow is undisturbed by the transducers. This methodology is consistent with the recommendations in IEC 60041 for isolating installation effects. The numerical scheme used for this integration is the same second-order accurate scheme used throughout the simulation. Compared to the reference position 2D upstream, the path lengths are shorter in this configuration. As a result, the axial velocity distribution in the measurement section is more constrained than that at the upstream 2D position. This distinct throttling effect enhances the flow velocity near the center of the pipeline. At the same time, a strong backflow forms adjacent to the upstream transducer, resulting in negative velocities at the upstream end of each path. Furthermore, the influence of lateral flow is also remarkably significant[13].

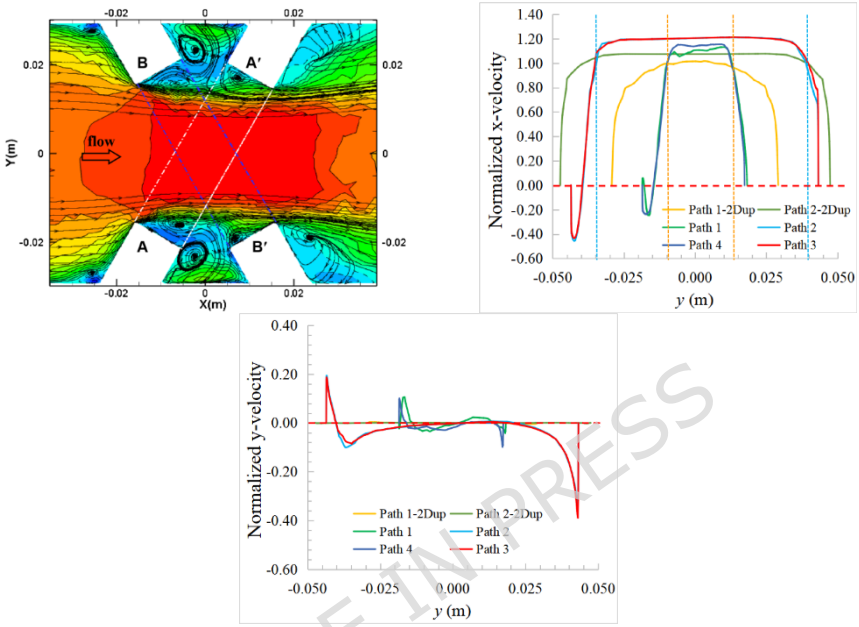

a. flow field distribution b. x-velocity c. y-velocity

Figure 4 Flow-field distribution and normalized velocity along four paths under fully projecting transducer installation mode.

In general, the flow along each path line can be divided into three distinct regions: the upstream reflux region, the middle flow region, and the downstream asymmetric region. The velocity loss integrated over the upstream backflow is defined as the influence error due to upstream transducer backflow. Similarly, the increase in velocity caused by flow throttling in the central region is termed the influence error of middle throttling. Lastly, the velocity loss resulting from flow asymmetry downstream is defined as the influence error of the downstream transducer. Together, these three types of velocity errors form the total velocity measurement error for each path. The distribution of axial velocity errors across different paths at a flow velocity of 20 m/s, under the fully projecting transducer installation mode, is provided in Table 4.

Table 4 Axial velocity error distribution at 20 m/s: fully projecting transducer installation mode

Path No.	Path length L_i' (mm)	Velocity weight factor W_i	Error of upstream transducer backflow (%)	Error of middle throttling (%)	Error of downstream transducer (%)	Total segmentation error (%)	Weighted error (%)	Total error (%)
1	42.5	0.1382	−20.85	24.54	−10.74	−7.05	−0.97	1.94
2	100.7	0.3618	−2.92	9.86	−1.92	5.02	1.82	
3	100.7	0.3618	−3.64	10.17	−1.45	5.08	1.84	
4	42.5	0.1382	−18.98	24.93	−11.33	−5.37	−0.74	

In calculating the linear average velocity V_i for each path, it is essential to account for the influence of both the lateral velocity V_{yi} and the axial velocity V_{xi}. Therefore, V_i should be computed using Equation 4. By comparing the flow velocity measured by the ultrasonic flowmeter with the upstream 2D reference condition, the velocity measurement error E_{sim} can

be determined. The variations of this error across different flow rates are summarized in Table 5.

Table 5 Velocity measurement error under fully projecting transducer installation mode

Inlet velocity (m/s)	Reynolds Number	Volumetric flow rate (m^3/h)	Reference velocity (m/s)	Calculated velocity (m/s)	Velocity measurement error (%)	Velocity correction error (%)
1	2.27E+03	28	0.99	0.98	−1.23	0.68
5	1.14E+04	141	4.95	4.87	−1.55	0.35
10	2.27E+04	282	9.88	9.72	−1.59	0.30
15	3.41E+04	424	14.83	14.55	−1.86	0.03
20	4.54E+04	565	19.78	19.42	−1.83	0.06
25	5.68E+04	707	24.72	24.39	−1.35	0.57
30	6.81E+04	848	29.67	29.33	−1.15	0.77

In the fully projecting transducer installation mode, the velocity measurement error remains consistently negative across various inlet velocities, primarily due to the effects of backflow and lateral flow. As the inlet velocity increases, the error fluctuates within a range of -1.15% to -1.86%. To mitigate this issue, we propose a velocity correction model[17] that incorporates both the actual path length L_i' and the ideal path length L_i (without backflow). This model is designed to correct the velocity measurement error for each path under the fully projecting installation mode, as expressed in Equation 5. In this equation, $\bar{v}_{ci}$ represents the corrected velocity for each path, $\bar{v}_{mi}$ denotes the simulated velocity, and n is the power exponent (where the velocity profile follows a $1/n$ exponential distribution, typically with n=10). The velocity measurement errors before and after correction are presented in Figure 5 and Table 5. The corrected error falls within approximately 0.03% to 0.77%, indicating a substantial improvement in accuracy.

$$\bar{v}_{ci} = \frac{1 - \frac{L_i - L_i'}{L_i}}{1 - \left(\frac{L_i - L_i'}{L_i}\right)^{1/n}} \bar{v}_{mi} \tag{5}$$

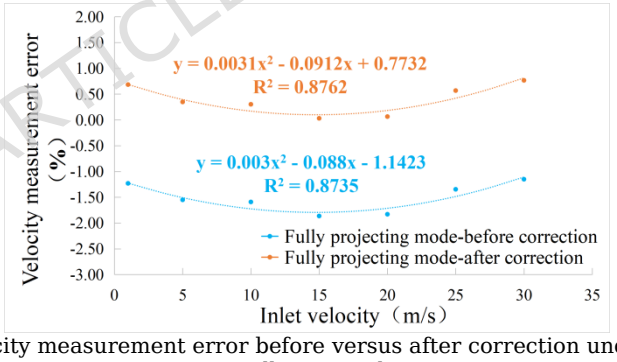

Figure 5 Comparison of velocity measurement error before versus after correction under fully projecting transducer installation mode.

3.2.2 Fully Recessed mode

In the fully recessed transducer installation mode, the fluid passes through the recessed cavities of both the upstream and downstream transducers. This flow induces backflow within the cavities, generating a region of negative pressure. As a result, vortices form inside the cavities, producing negative velocities at the endpoints of each acoustic path. These effects collectively lead to negative measurement errors, as shown in Figure 6.

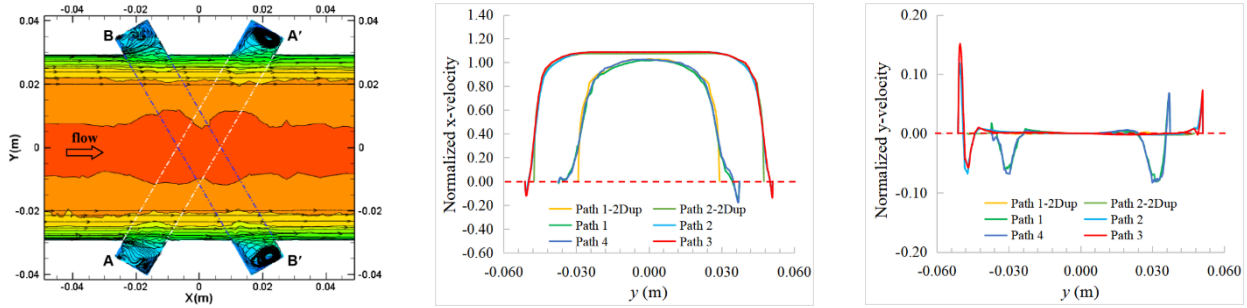

a. Vortex distribution b. x-velocity c. y-velocity

Figure 6 Vortex and normalized velocity distribution along four paths under fully recessed transducer installation mode.

In the fully recessed transducer installation mode, the presence of recessed grooves increases the flow area—a key distinction from the fully projecting mode. This expansion contributes to a negative velocity measurement error within the central expanded region. As the distance between the transducer and the pipeline axis grows, the installation groove becomes deeper, resulting in a progressively more negative flow velocity measurement error, which is consistent with the actual simulation results. Since the errors in the upstream, middle, and downstream segments are all negative, this installation method yields the largest measurement error among the three techniques. Specifically, at a flow velocity of 20 m/s, the error reaches -10.35%, as shown in Table 6. It is crucial to emphasize that this -10.35% figure represents the raw, uncorrected error from the simulation, quantifying the isolated impact of severe flow distortion. It is not the final uncertainty of a calibrated flowmeter. After applying the correction model proposed in this section, this error is reduced to within ±1% (as shown in Table 7 and Figure 7), which is more representative of a calibrated meter's performance.

Table 6 Axial Velocity Error Distribution at 20 m/s: Fully Recessed Transducer Installation Mode

Path No.	Path length L_i' (mm)	Velocity weight factor W_i	Error of upstream transducer backflow (%)	Error of middle throttling (%)	Error of downstream transducer (%)	Total segmentation error (%)	Weighted error (%)	Total error (%)
1	86.4	0.1382	□6.29	□7.71	□6.89	□20.89	□2.89	□10.35
2	117.9	0.3618	□2.09	□2.30	□2.12	□6.50	□2.35	
3	117.9	0.3618	□1.91	□2.12	□2.15	□6.18	□2.24	
4	86.4	0.1382	□5.94	□7.99	□6.84	□20.78	□2.87	

The influence of lateral flow velocity on each path is considerable, as indicated by the measurement errors under the fully recessed transducer installation mode (see Table 7). Notably, the velocity measurement error decreases as the inlet velocity rises. This trend implies that the effect of transducer-induced turbulence becomes more pronounced at higher flow velocities.

Table 7 Velocity measurement error under fully recessed transducer installation mode

Inlet velocity (m/s)	Reynolds Number	Volumetric flow rate (m^3/h)	Reference velocity (m/s)	Calculated velocity (m/s)	Velocity measurement error (%)	Velocity correction error (%)
1	2.27E+03	28	0.99	0.90	□9.66	1.31
5	1.14E+04	141	4.95	4.46	□9.95	0.84
10	2.27E+04	282	9.88	8.88	□10.15	0.42
15	3.41E+04	424	14.83	13.30	□10.33	0.24
20	4.54E+04	565	19.78	17.71	□10.48	0.09
25	5.68E+04	707	24.72	22.12	□10.53	0.03
30	6.81E+04	848	29.67	26.54	□10.57	□0.01

In the fully recessed transducer installation mode, a velocity correction model is proposed based on the actual path length L_i' and the reference path length L_i, as expressed in Equation 6. The velocity measurement errors before and after correction are shown in Figure 7 and Table 7.

$$\overline{V}_c = \frac{L_i'}{L_i}\overline{V}_m \quad (6)$$

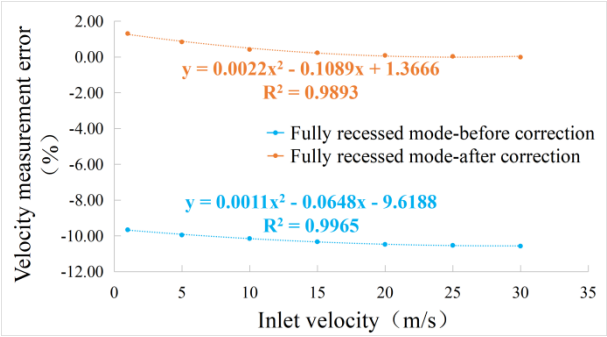

Figure 7 Comparison of velocity measurement error before and after correction under fully recessed transducer installation mode.

3.2.3 Tangent mode

Figure 8 shows the velocity distributions under the tangent transducer installation mode, which are similar to those observed in the fully projecting mode. However, since the actual path length matches the reference path length, that is $L_i \approx L_i'$, the relative extent of the reflux region is reduced. As a result, the errors caused by upstream transducer backflow, middle throttling, and downstream transducer effects are all numerically diminished.

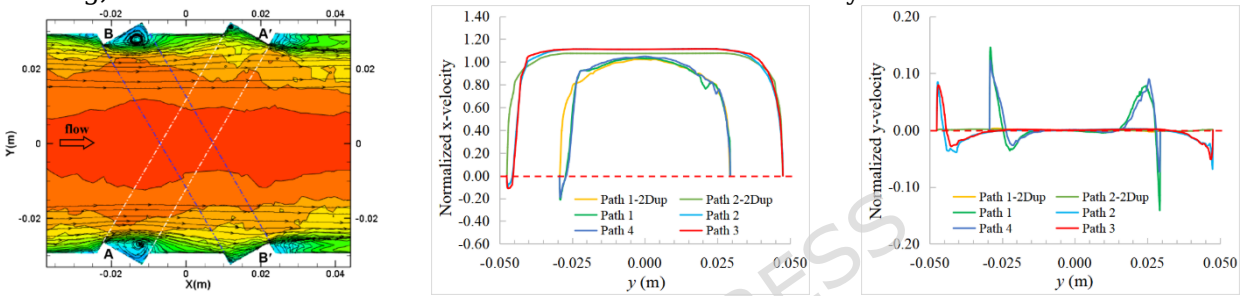

a. Vortex distribution b. x-velocity c. y-velocity

Figure 8 Normalized velocity distribution along four paths for tangent transducer installation mode.

In terms of proportion, the error attributable to upstream transducer backflow increases to three times that of the downstream transducer error, thereby replacing the middle throttling error as the dominant source of inaccuracy. As a result, the cumulative weighted errors for each path are negative. At a flow velocity of 20 m/s, the velocity measurement error reaches -2.4%, as summarized in Table 8.

Simulation results across the three installation modes consistently indicate that the influence of the ultrasonic transducer installation effect intensifies with increasing distance of the acoustic path from the pipeline axis. Therefore, the installation effect has a more pronounced impact on paths 1 and 4 than on paths 2 and 3.

Table 8 Axial velocity error distribution at 20 m/s: tangent transducer installation mode

Path No.	Path length L_i' (mm)	Velocity weight factor W_i	Error of upstream transducer backflow (%)	Error of middle throttling (%)	Error of downstream transducer (%)	Total segmentation error (%)	Weighted error (%)	Total error (%)
1	67.9	0.1382	−7.75	4.55	−2.56	−5.76	−0.80	−2.40
2	109.8	0.3618	−1.41	0.86	−0.25	−0.80	−0.29	
3	109.8	0.3618	−1.95	1.14	−0.58	−1.39	−0.50	
4	67.9	0.1382	−7.19	3.51	−2.15	−5.83	−0.81	

In the tangent transducer installation mode, the influence of lateral velocity on velocity measurement error decreases monotonically as the inlet velocity increases, as shown in Table 9. This indicates that transducer-induced turbulence exerts a stronger effect at higher inlet velocities—a trend consistent with that observed in the fully recessed installation mode. However, the error diminishes more rapidly in the tangent mode.

Table 9 Velocity measurement error under tangent transducer installation mode

Inlet velocity (m/s)	Reynolds Number	Volumetric flow rate (m^3/h)	Reference velocity (m/s)	Calculated velocity (m/s)	Velocity measurement error (%)	Velocity correction error (%)
1	2.27E+03	28	0.99	0.95	−2.26	−0.81

5	1.14E+04	141	4.95	4.70	−2.88	−1.44
10	2.27E+04	282	9.88	9.36	−3.42	−1.98
15	3.41E+04	424	14.83	13.99	−3.62	−2.19
20	4.54E+04	565	19.78	18.65	−3.87	−2.44
25	5.68E+04	707	24.72	23.26	−3.97	−2.54
30	6.81E+04	848	29.67	27.87	−4.09	−2.67

In the tangent installation mode $h = d/2\cos\beta$, if the chord length at the corresponding position of each path is denoted as D_i', and the diameter of the transducer is represented by d, then the protrusion height of the transducer, h, can be determined. We introduce a velocity correction model that takes into account the actual flow width, defined as $(D_i' - 2h)$, as illustrated in Equation 7. The discrepancies in flow velocity measurements before and after this correction are detailed in Table 9 and depicted in Figure 9.

$$\bar{v}_{ci} = \frac{1-\frac{D_i'-2h}{D_i'}}{1-\left(\frac{D_i'-2h}{D_i'}\right)^{\frac{1}{n}}}\bar{v}_{mi} = \frac{1-\frac{L_i\sin\beta - d\cos\beta}{L_i\sin\beta}}{1-\left(\frac{L_i\sin\beta - d\cos\beta}{L_i\sin\beta}\right)^{\frac{1}{n}}}\bar{v}_{mi} \tag{7}$$

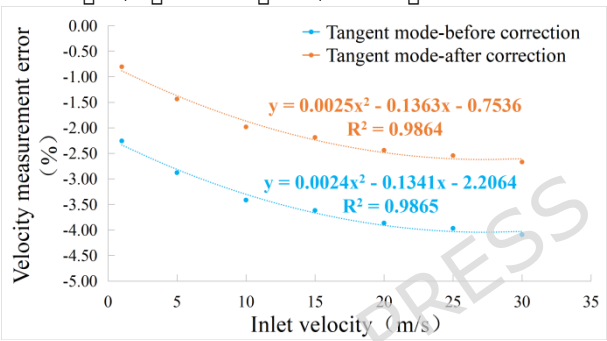

Figure 9 Comparison of velocity measurement error before and after correction under tangent transducer installation mode.

3.3 Comparison of measurement errors of simulation results under different transducer installation modes

A comparison of three common transducer installation modes reveals that negative measurement errors consistently occur at both ends of each acoustic path, irrespective of the differing flow field mechanisms involved. These errors lead to measured velocities that are consistently lower than the actual values.

As shown in Figure 10, the fully projecting installation mode has the least influence on each path and thus results in the smallest velocity measurement error[7, 18]. In contrast, the fully recessed mode considerably disturbs the flow, resulting in the largest overall velocity measurement error (Figure 10a). Nevertheless, when either fully projecting or fully recessed transducers are used, the velocity correction proves highly effective: after adjustment, errors are generally confined within ±1%, as demonstrated in Figure 10b.

In the tangent transducer installation mode, the initial velocity correction is often insufficient, making additional flow compensation necessary. Further experimental investigations on this topic will be presented in Section 4.

During flow measurement, the influence of acoustic path length must be carefully considered. Parameters such as the protrusion or recess depth of the transducers should be determined through comprehensive real-flow calibration experiments. These parameters must also be integrated with the flow field compensation algorithm of the ultrasonic flowmeter in practical engineering applications.

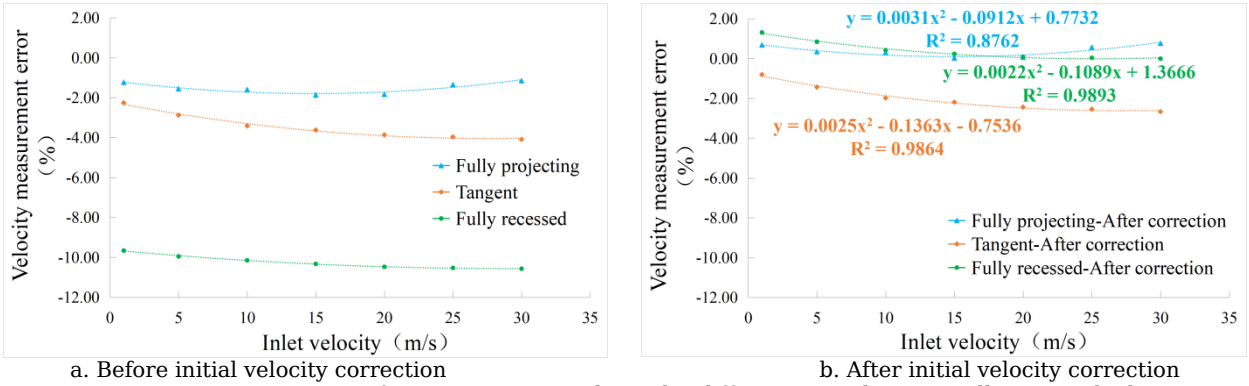

a. Before initial velocity correction b. After initial velocity correction

Figure 10 Comparison of measurement results under different transducer installation methods.

4. Experimental results and error correction model of ultrasonic flowmeter with tangent transducer installation

In fully developed flow, the velocity correction coefficient, denoted as k, can be used to improve the accuracy of velocity conversion—particularly when transforming linear average velocities from individual paths into a surface average velocity. The determination of this coefficient in multi-path ultrasonic flowmeters should account for factors such as the number of paths, transducer installation position, and velocity distribution. Additionally, flow correction may be enhanced through a combination of linear or nonlinear fitting methods.

The influence of local flow field distortion caused by the transducer on the measurement performance of an ultrasonic flowmeter is investigated through numerical simulation. This section describes the calibration of an ultrasonic flowmeter with tangent-mode transducer installation using a real-flow experiment. The validity of the velocity correction model is also verified. Furthermore, an additional error correction model based on Reynolds number is proposed to improve the measurement accuracy of the ultrasonic flowmeter.

In the high-pressure closed-loop working standard facility, two ultrasonic flowmeters with diameters of 100 mm and 200 mm were selected for real-flow tests under different pressure conditions[19]. The DN100 diameter was selected for the numerical simulations to enable direct validation against experimental data obtained from our standard calibration facilities, which are equipped with DN100 and DN200 flowmeters. While extending the analysis to smaller diameters, such as DN50, would be valuable for understanding scale effects, it falls outside the scope of the current experimental setup and is planned for future work. The experimental results and initial correction outcomes for the DN100 mm ultrasonic flowmeter are shown in Figure 11. The errors caused by local transducer turbulence in the DN100 mm flowmeter were consistently negative, ranging from -3.0% to -1.5%, which aligns with the simulation findings. After initial correction using Equation 7, the errors were reduced to a range of -1.54% to -0.02%, as illustrated in Figure 11a. Nevertheless, the post-correction accuracy still fails to meet the required measurement standards for the ultrasonic flowmeter, indicating the need for further error compensation[20].

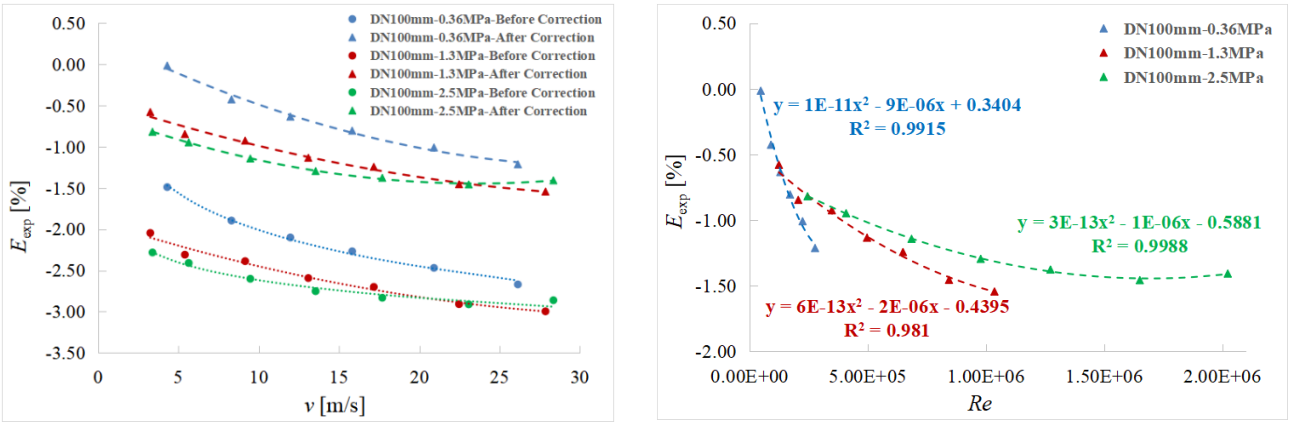

a. Experimental results and the error after initial correction based on Reynolds Number b. The further error correction model

Figure 11 The experimental results of DN100mm ultrasonic flowmeter on high pressure air flow standard device.

The results are presented as a function of flow rate (m^3/h) and pressure (MPa) to directly reflect the controlled parameters of the high-pressure loop facility. For a more generalized analysis applicable across different scales and fluid properties, the corresponding Reynolds numbers are provided in Table 10. In practical applications of

ultrasonic flowmeters, the state of the flow field under stable conditions can be evaluated by monitoring the Reynolds number. This value offers a specific correction coefficient that reflects variations in the flow field. The comprehensive correction coefficient, denoted as K_1, can be obtained by fitting the measurement error to the Reynolds number using experimental data. As shown in Figure 11b, the fitted relationship between measurement error and Reynolds number follows a polynomial trend. Accordingly, the Reynolds number-based correction coefficient is expressed by Equation 8:

$$K_1 = aRe^2 + bRe + c \quad (8)$$

Table 10 Corrected error of DN100mm ultrasonic flowmeter

0.36 MPa		1.3 MPa		2.5 MPa	
Reynolds Number	Error after correction (%)	Reynolds Number	Error after correction (%)	Reynolds Number	Error after correction (%)
4.67E+04	−0.023	1.23E+05	−0.015	2.45E+05	0.001
8.99E+04	−0.006	2.05E+05	−0.057	4.08E+05	0.032
1.29E+05	0.043	3.47E+05	0.093	6.85E+05	0.002
1.71E+05	0.039	4.96E+05	0.042	9.77E+05	−0.038
2.24E+05	0.011	6.49E+05	0.051	1.27E+06	−0.036
2.76E+05	−0.052	8.43E+05	−0.044	1.65E+06	−0.035
		1.04E+06	−0.042	2.02E+06	0.078

As shown in Figure 12, the error caused by local flow field distortion in the transducer of the DN200 mm ultrasonic flowmeter is primarily negative, ranging from –2.03% to –1.31%. Compared with the experimental results from the DN100 mm flowmeter, the influence of local turbulence is less significant in the DN200 mm unit. This indicates that transducer-induced flow interference has a stronger effect in smaller-diameter pipes. After initial correction using Equation 7, the errors are reduced to between –0.69% and 0.04%, as illustrated in Figure 12a. The data indicate that the measurement accuracy of the DN200 mm ultrasonic flowmeter under various pressure conditions meets acceptable levels after the initial correction. Moreover, these results suggest that larger pipe diameters improve the efficacy of the initial correction for transducer-related local flow distortions.

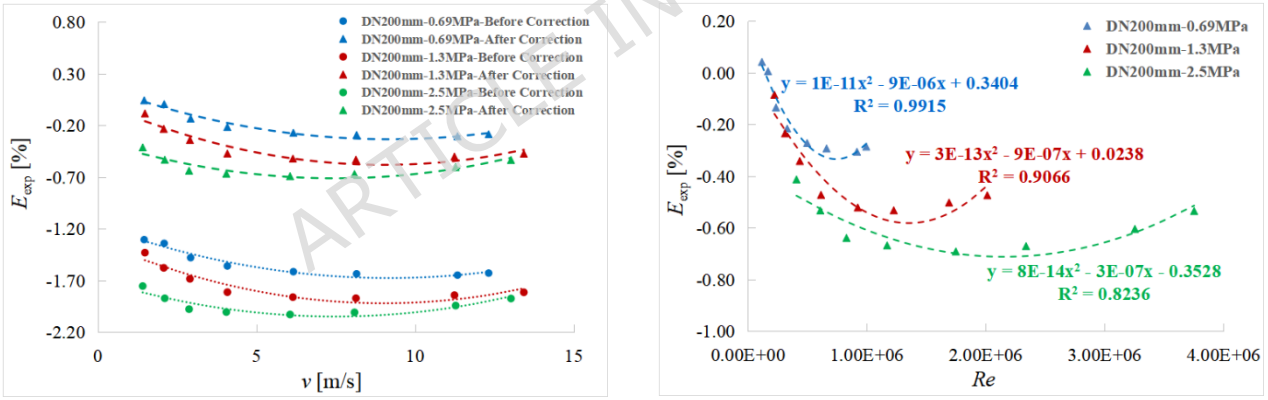

a. Experimental results and the error after initial correction based on Reynolds Number

b. The further error correction model

Figure 12 The experimental results of DN200mm ultrasonic flowmeter on high pressure air flow standard device.

The positive slope observed in the post-correction error for the DN200 mm meter at high Reynolds numbers in Figure 12b warrants discussion. This trend may be attributable to two potential factors: (1) it could be an artifact of the polynomial fitting applied to a limited dataset at the extreme of the tested Reynolds number range, or (2) it may indicate that the assumptions of our correction model begin to break down at very high flow rates, where other phenomena (e.g., compressibility effects or changes in the turbulence structure) may become non-negligible. Further experimental data in this high-Re region are required to validate and refine the correction model. The error after the initial correction of the DN200 mm ultrasonic flowmeter also exhibits a polynomial fitting relationship with the Reynolds number. The error values obtained after the second correction, computed using Equation 8, are summarized in Table 11.

Table 11 Corrected error of DN200mm ultrasonic flowmeter

0.69 MPa		1.3 MPa		2.5 MPa	
Reynolds Number	Error after correction	Reynolds Number	Error after correction	Reynolds Number	Error after correction

	(%)		(%)		(%)
1.18E+05	−0.029	2.23E+05	0.076	4.08E+05	0.049
1.69E+05	−0.027	3.12E+05	−0.005	6.09E+05	−0.025
2.36E+05	−0.123	4.36E+05	−0.028	8.29E+05	−0.089
3.30E+05	−0.157	6.15E+05	−0.052	1.17E+06	−0.070
4.98E+05	−0.169	9.24E+05	0.035	1.75E+06	−0.055
6.61E+05	−0.197	1.23E+06	0.102	2.34E+06	−0.050
9.17E+05	−0.317	1.69E+06	0.142	3.25E+06	−0.120
9.96E+05	−0.354	2.02E+06	0.110	3.75E+06	−0.181

In conclusion, the modified model developed in this study accounts for the interaction between transducer-induced local flow field disturbances and the turbulent characteristics in a circular pipe. The methodology presented here provides a framework for estimating and correcting these effects. However, it is important to emphasize that the quantitative correction factors derived in this study are specific to the geometries and conditions investigated. For high-precision applications, site-specific or diameter-specific calibration remains necessary, as the correction factors may not be universally applicable without further validation. It is important to note that under complex flow conditions, changes in the flow field cannot be fully characterized by the Reynolds number alone. A more refined classification of flow regimes is therefore necessary.

5. Conclusion

In this study, simplified physical models of ultrasonic flowmeters are developed for three transducer installation modes: fully projecting, fully recessed, and tangent. The SST *k*-omega turbulence model is employed to simulate the separated flow fields induced by the transducer. We examine the physical mechanisms through which local flow field distortions near the transducer influence measurement accuracy across these common installation configurations.

The flow region along each acoustic path is divided into three distinct sections: the upstream reflux region, the middle flow region, and the downstream asymmetric region. Velocity errors originating from these regions collectively contribute to the total velocity measurement error of the path. Through detailed analysis of error distributions in different flow regions, installation-dependent patterns of measurement error are identified. Based on these findings, a tailored error correction model for velocity measurement is proposed.

The ultrasonic flowmeter with tangent transducer installation mode was further calibrated through real-flow experiments. The results indicate that the errors induced by transducer-induced local flow field distortion are consistently negative, which aligns well with the simulation findings. It is noteworthy that the influence of this distortion becomes more pronounced as the flowmeter diameter decreases. Based on experimental data, a polynomial error correction model dependent on the Reynolds number was developed via data fitting. This modified model demonstrates strong applicability across different pressures and flowmeter diameters. These findings provide a theoretical basis for transducer installation and operation in small to medium-diameter ultrasonic flowmeters. Furthermore, the simulation approach presented in this study may serve as a reference for addressing similar types of flow measurement challenges.

It is important to emphasize the limitations and future directions of this work. First, this CFD model is primarily focused on hydrodynamic effects and does not consider acoustic wave propagation or piezoelectric interactions. Second, while this study focused on simplified cylindrical transducers, real-world transducers often feature radial grooves and rounded edges. Future work should investigate the impact of these geometric details on the local flow field. Third, extending the analysis to a wider range of pipe diameters (e.g., DN50) and installation angles would provide a more comprehensive understanding of transducer installation effects. Fourth, the transition from low-pressure air to high-pressure natural gas, particularly across the laminar-turbulent transition range, is another critical area for future investigation. Finally, while the correction models proposed are effective for the specific geometries studied, their coefficients are not universally transferable; site-specific calibration remains necessary for final accuracy in high-precision applications. Future work should also investigate the application of more sophisticated integration methods, such as OWICS (Optimized Weights for Circular Section), which may offer improved accuracy by better accounting for realistic velocity profiles in the presence of installation effects. Additionally, extending the analysis to a wider range of pipe diameters and exploring the transition from low-pressure air to high-pressure natural gas, particularly across the laminar-turbulent transition range, remain important directions for future research.

CRediT authorship contribution statement

Wenlin Chen: Investigation, Supervision, Methodology, Writing - original draft & editing. Cunxin Yao: Writing & editing. Duoyong Wang: Conceptualization. Jun Mu: Methodology, Writing - review & editing. Chao Xu and Defu Xu: Data curation.

Declaration of competing interest

The authors declare that they have no known competing financialinterests or personal relationships that could have appeared to influence the work reported in this paper.

Data availability

The data supporting the findings of this study are available upon request from the corresponding author.

Funding

The work was supported by the Xinjiang Talent Development Fund (Grant No.: XJRC-2025-GX-PY-GCS-002), as well as the Natural Science Foundation of Xinjiang Uygur Autonomous Region (Grant No.: 2025D01A81) and the Science and Technology Program of Xinjiang Institute of Measurement and Testing Technology (Grant No.: XJL2024KY006).

References

[1] American Gas Association, Measurement of gas by multipath ultrasonic meters[S]. 1998.
[2] Voser A., Staubli T. CFD-Calculations of the protrusion effect and impact on the acoustic discharge measurement accuracy[C]. in Proceedings. 1996.
[3] Drenthen J .G., de Boer G. The manufacturing of ultrasonic gas flow meters[J]. Flow Measurement and Instrumentation, 2001. 12(2): 89-99.
[4] Zhao N., Hu L., Peng X., Fang Z., Chen W., Fu X. A method combining measurement tool and numerical simulation for calculating acoustic signals of ultrasonic flowmeter[J]. IEEE Sensors Journal, 2019. 19(24): 11805-11813.
[5] Zhao H., Peng L., Stephane S.A., Ishikawa H., Shimizu K., Takamoto M. CFD Aided Investigation of Multipath Ultrasonic Gas Flow Meter Performance Under Complex Flow Profile[J]. IEEE Sensors Journal, 2014. 14(3): 897-907.
[6] International Electrotechnical Commission, Field Acceptance Tests to Determine the Hydraulic Performance of Hydraulic Turbines, Storage Pumps and Pump-turbines[M]. 1991.
[7] Zheng D., Zhang P., Xu T. Study of acoustic transducer protrusion and recess effects on ultrasonic flowmeter measurement by numerical simulation[J]. Flow Measurement and Instrumentation, 2011. 22(5): 488-493.
[8] Wang B., Cui Y., Liu W., Luo X. Study of Transducer Installation Effects on Ultrasonic Flow Metering Using Computational Fluid Dynamics[J]. Advanced Materials Research, 2013. 629: 676-681.
[9] Lowell F., Schafer S., Walsh J. Acoustic flowmeters in circular pipes: Acoustic transducer and conduit protrusion effects in discharge measurement[C]. in the International Group for Hydraulic Efficiency Measurement 98. 1998.
[10] Renaldas R. Investigation of the flow velocity profile in a metering section of an invasive ultrasonic flowmeter[J]. Flow Measurement and Instrumentation, 2006. 17(4): 201-206.
[11] Roman V., Matiko F., Kostyk I. Investigation of Turbulence Parameters Influence on Results of CFD Modeling of Flow in Ultrasonic Flowmeter[J]. Energy Engineering and Control Systems, 2021. 7(1): 73-78.
[12] Wiranata L. F., Kurniadi D. The development of simultaneous transducer ultrasonic with dual-transducer to measure flow velocity in the pipe[J]. EUREKA: Physics and Engineering, 2023(4): 77-86.
[13] Arnould P. An investigation into the performance and diagnostics from different chordal integration schemes in asymmetric flow[J]. Flow Measurement and Instrumentation, 2020. 72: 101644.
[14] Guo S., Xiang N., Li B., Wang F., Zhao N., Zhang T. Integration method of multipath ultrasonic flowmeter based on velocity distribution[J]. Measurement, 2023. 207: 112388.
[15] Roman V., Matiko H., Kostyk I., Pistun O. Mathematical model of multipath ultrasonic flowmeter for its automated designing[C]. in 2021 Selected Issues of Electrical Engineering and Electronics (WZEE). 2021. IEEE.
[16] Pannell C., Evans W., Jackson D., A new integration technique for flowmeters with chordal paths[J]. Flow measurement and Instrumentation, 1990. 1(4): 216-224.

[17] Zhang L., Meng T., Wang C., Hu H., Qin C. Probe installation effects on the accuracy of feed thru ultrasonic flowmeters[J]. Chinese Journal of Scientific Instrument, 2012. 33(10): 2307-2314.
[18] Liu D., Cai Q., Hu H. Laboratory Test and Optimization of Ultrasonic Flow Measurement Device[J]. Acta Metrologica Sinica, 2021. 42(10): 1282-1287.
[19] Wang C., Li C., Xu M., Yan W. The high pressure close loop gas flow standard facility in NIM[C]. in Proceedings of the Flomeko. 2019.
[20] Yu X., Xu K. Calculation and judgment of repeatability error affected by non-linearity correction based on flowmeter characteristic analysis[J]. Measurement, 2022. 196: 111251.